Tellus (1982), *34*, 588–600

Simulation of laboratory vortex flow by axisymmetric similarity solutions

By WILLIAM H. RAYMOND and H. L. KUO *Department of Geophysical Sciences The University of Chicago, Chicago, Illinois 60637, U.S.A.*

(Manuscript received August 17, 1981; in final form March 3, 1982)

ABSTRACT

A similarity approach is utilized to investigate a simple axisymmetric steady-state model of the convergence region of a laboratory vortex. The resulting simplified set of equations are solved for a range of swirl angles by varying the tangential or radial velocity component at the outer rim. By increasing the swirl angle the flow is found to go from a one cell to a two cell configuration, i.e., the vertical velocity changes from everywhere positive to negative in the vicinity of the axis. Correspondingly the vertical vorticity maximum moves from the axis outward toward the radius of maximum tangential velocity, making the flow barotropically unstable with respect to unsymmetrical perturbations.

1. Introduction

A variety of rotating or swirling motions are observed in the atmosphere. Of particular interest in this study are the dynamically dominated tornadic type vortices. Various theories on the nature of the internal dynamics within these strong vortex flows have been discussed (e.g., see Davies-Jones and Kessler, 1974), but actual measurements are almost impossible to obtain due to the severity of the motions. To help answer some of the major questions, a number of laboratory vortex experiments have been conducted, e.g., Turner and Lilly (1963), Ying and Chang (1970), Ward (1972), Jischke and Parang (1974), Leslie (1977), Church *et al.* (1977), etc. Beginning with Ward (1970, 1972), one of the advantages of the modern vortex generator is its ability to reproduce the multiple vortex phenomena in an environment where it can be intensely studied. Fujita (1971, 1972) first proposed that the cycloidal markings observed in tornado damage paths are produced by these secondary rotations. The presence of multiple vortices within some tornadoes has now been widely accepted and analysed in various studies, e.g. Agee *et al.* (1975) and Forbes (1978).

Because of the success of the laboratory simulations, a few elaborate numerical reproductions of the vortex generator have been attempted, e.g., Harlow and Stein (1974) and Rotunno (1977, 1979). These studies certainly have helped to identify various features of the dynamics, but questions still remain, e.g., what is the relationship between the vertical motion near the axis and the inflow angle at a large distance from the axis, and what is the nature of the instability that allows multiple vortices to generate. To help refine answers to these and other questions, a simple analytical-numerical steady-state model is investigated.

2. Formulation of the problem

Our goal is to simulate in a simple manner a steady-state vortex similar to those produced in modern laboratory vortex generators and to study its behavior. These laboratory vortices are created mechanically in a specially designed arrangement which contains an exhaust fan and a rotating screen. Air is drawn radially inward by the fan through the rotating screen till it reaches a central cylinder where it is allowed to rise through the cylinder and is expelled at the top.

The rotating screen imparts a background

0040-2826/82/060589-13$02.50/0

angular momentum which is nearly conserved as the air moves radially inward giving rise to a concentrated vortex core. The laboratory experiment is constructed so that it is geometrically and dynamically similar to conditions found in the atmosphere during, for example, a tornadic event. This similarity is established by requiring that the non-dimensional numbers that govern the flow in the mechanically generated vortex be in the same range as those observed in the atmosphere. Lewellen (1962) found three nondimensional parameters that govern the nature of the swirling flow. These are: the radial Reynolds number

$Re_r = Q/2\pi\nu$,

an internal aspect ratio

$a = H/R$,

and a swirl ratio

$S = \tan\theta/2a$.

Here Q is the volume flow rate per unit axial length, ν is the viscosity coefficient, H the inflow depth, R the radius of convergence and θ is the swirl or inflow angle. It is known that the swirl ratio and radial Reynolds number describe the dynamics of the flow while the aspect ratio describes the geometry.

If all three of these numbers are of equal importance then the geometry of the simulator would have to be considered and/or duplicated in any numerical simulation. Davies-Jones (1973) however points out that the nature of the swirling flow is dominated by the swirl ratio. Because of this there is some hope that a restricted investigation ignoring the geometry and only dealing with just part of the vortex simulator, e.g. the region where convergence takes place, might be successful in explaining some of the general behaviour that is observed in the laboratory vortex and thus consequently in the atmosphere. It is in this context that we adopt a similarity approach to simplify the governing equations. The procedure has been orchestrated so that we can examine the vortex flow configuration, as described in the simplified similarity equations, for a range of swirl angles.

3. The mathematical development

Assuming that the motion of the homogeneous fluid is steady and axisymmetric and that the Coriolis force can be neglected in comparison with the centrifugal force, then the swirling flow satisfies the following equations of motion in cylindrical coordinates (Kuo, 1966, 1969):

$$u\left(\frac{\partial v}{\partial r} + \frac{v}{r}\right) + w\frac{\partial v}{\partial z} = \nu\nabla_1^2 v, \tag{1}$$

$$u\frac{\partial u}{\partial r} + w\frac{\partial u}{\partial z} - \frac{v^2}{r} = -\frac{1}{\rho}\frac{\partial p}{\partial r} + \nu\nabla_1^2 u, \tag{2}$$

$$u\frac{\partial w}{\partial r} + w\frac{\partial w}{\partial z} = -\frac{1}{\rho}\frac{\partial p}{\partial z} - g + \nu\left(\nabla_1^2 w + \frac{w}{r^2}\right), \tag{3}$$

$$\frac{\partial(ur)}{\partial r} + r\frac{\partial w}{\partial z} = 0, \tag{4}$$

where

$$\nabla_1^2(\,) = \frac{\partial}{\partial r}\frac{1}{r}\frac{\partial r(\,)}{\partial r} + \frac{\partial^2}{\partial z^2}(\,).$$

r is the radial coordinate, z the vertical coordinate positive in the direction opposite to the gravitational acceleration represented by g, and u, v and w are the radial, the tangential and the axial component of velocity, p is the pressure and ρ is the density.

The velocity components u and w can be expressed in terms of the stream function ψ defined by

$$u = -\frac{1}{r}\frac{\partial\psi}{\partial z}, \qquad w = \frac{1}{r}\frac{\partial\psi}{\partial r}. \tag{5a,b}$$

From eqs. (2) and (3) we obtain the following equation for the azimuthal vorticity

$$\zeta \equiv \frac{\partial w}{\partial r} - \frac{\partial u}{\partial z} = \nabla_1^2(\psi/r), \tag{6a}$$

$$\frac{\partial\psi}{\partial r}\frac{\partial}{\partial z}(\zeta/r) - \frac{\partial\psi}{\partial z}\frac{\partial}{\partial r}(\zeta/r) + \frac{2v}{r}\frac{\partial v}{\partial z} = \nu\nabla_1^2\zeta. \tag{6b}$$

Eqs. (6b) and (1) together form a closed system for the dependent variables v and ψ (after using (5a,b) and (6a) to eliminate u, w and ζ).

3.1. *A similarity approach*

Following in the spirit of the similarity approaches utilized by Kuo (1966, 1969) the variables are first non-dimensionalized by the following transformations:

$$\psi = U_s r_s h \psi^*, \qquad z = hz^*$$

$$m = U_s r_s m^*, \qquad v = U_s r_s v^* \quad \text{and} \quad x = r^2/4r_0^2. \tag{7}$$

Here r_s is the radius of the rotating screen at the outer edge or rim, h is a measure of the effective depth, r_o is some measure in the radial direction and U_s is the radial velocity at the rim while $m = vr$ denotes the angular momentum. Note that v^*, ψ^*, m^*, z^* and x are all dimensionless.

The dimensionless equivalent of eq. (1) when written in terms of m^* becomes

$$-\frac{\partial\psi^*}{\partial z^*}\frac{\partial m^*}{\partial z} + \frac{\partial\psi^*}{\partial x}\frac{\partial m^*}{\partial z^*} = 2v^*\left[x\frac{\partial^2 m^*}{\partial x^2} + \delta^{-1}\frac{\partial^2 m^*}{\partial z^{*2}}\right], \tag{8}$$

while eq. (6b) reduces to

$$m^*\frac{\partial m^*}{\partial z^*} = \delta x^2\left[2v^*\frac{D^4\psi^*}{x} - \frac{\partial\psi^*}{\partial x}\left(\frac{D^2\psi^*}{x}\right)_{z^*} + \frac{\partial\psi^*}{\partial z^*}\left(\frac{D^2\psi^*}{x}\right)_x\right], \tag{9}$$

where the subscripts z^* and x denote partial differentiations and

$$\delta = h^2 r_0^{-2}, \qquad D^2\psi^* = x\frac{\partial^2\psi^*}{\partial x^2} + \delta^{-1}\frac{\partial^2\psi^*}{\partial z^{*2}}$$

and $D^4\psi^* = D^2(D^2\psi^*)$. Observe from (9) that the meridional flow is influenced by m^* only through the variation of m^* with z^*. To include this effect, we follow again the basic premise established by Kuo (1966, 1969) by expanding the flow variables in power series expansions in z^* and including the zeroth order terms m_0 and u_0 in m^* and u^*. It can readily be shown that only the even order terms of z^* in m^* and u^* will contribute to these two variables and therefore we write m^* and ψ^* in the following forms

$$m^* = v^*[m_0 + \delta z^{*2} m_1 + (\delta z^{*2})^2 m_2 + \cdots], \tag{10}$$

$$\psi^* = 2v^* z^*[F_0 + \delta z^{*2} F_1 + (\delta z^{*2})^2 F_2 + \cdots]. \tag{11}$$

Both m^* and ψ^* will be well defined provided the higher order terms are decreasing in importance.

From eqs. (5a,b), (7), (10) and (11) we arrive at the following expressions for u, w and m:

$$u = -\frac{2v}{r}[F_0 + 3\delta z^{*2}F_1 + 5(\delta z^{*2})^2 F_2 + \cdots], \tag{12}$$

$$w = \frac{vz}{r_0^2}[F_0' + \delta z^{*2}F_1' + (\delta z^{*2})^2 F_2' + \cdots], \tag{13}$$

$$m = vr = v[m_0 + \delta z^{*2} m_1 + (\delta z^{*2})^2 m_2 + \cdots]. \tag{14}$$

The prime denotes differentiation with respect to x.

Using the expansions in (10) and (11) in eqs. (8) and (9) and by setting the coefficients of the individual powers of δ to zero, the partial differential equations are transformed into a system of coupled ordinary differential equations with independent variable x which is proportional to r^2. From the angular momentum equation (8), we obtain for m_0 and m_1 the second order differential equations

$$xm_0'' + F_o m_0' = -2m_1, \tag{15}$$

$$xm_1'' + F_0 m_1' - 2F_0' m_1 = -3F_1' m_0' - 12m_2. \tag{16}$$

From the vorticity equation (9), we find that F_0 and F_1 are each defined by a fourth order differential equation,

$$[xF_0''' + (1 + F_0)F_0'' - F_0'^2 + 12F_1']' = \frac{m_0 m_1}{2x^2} - 6F_0^2\left(\frac{F_1}{xF_0}\right)' - \frac{120F_2}{x}, \tag{17}$$

$$[XF_1''' + (1 + F_0)F_1'' - 4F_0'F_1' + 3F_0''F_1]' + 6x^2\left(\frac{F_1^2}{x^3}\right)' = \frac{1}{x^2}(m_0 m_2 + \tfrac{1}{2}m_1^2) - 20F_0\left(\frac{F_2}{x}\right)' + 60\frac{F_0'F_2}{x} - 40F_2'' - \frac{840F_3}{x}. \tag{18}$$

Equations for the higher order terms in (10) and (11) can also be obtained but are not presented here. The system of equations becomes closed for any given cut-off limit.

3.2. *Solution by perturbation expansion*

Instead of treating the system of highly coupled nonlinear equations (15)–(18) directly, we shall solve them by expanding the dependent variables in powers of a coupling parameter α so as to separate the most fundamental part $F_{00}(x)$ of $F_0(x)$ in (17) from the other variables to make F_{00} satisfy an uncoupled equation, and obtain the coupling parts of the various functions by successive approximation. The expansions which serve this purpose can be written as

$$F_0 = F_{00} + \alpha F_{01} + \alpha^2 F_{02} + \cdots, \tag{19}$$

$$m_0 = m_{00} + \alpha m_{01} + \alpha^2 m_{02} + \cdots,$$

$$F_1 = \alpha F_{10} + \alpha^2 F_{11} + \alpha^3 F_{12} + \cdots,$$

$$m_1 = \alpha m_{10} + \alpha^2 m_{11} + \alpha^3 m_{12} \cdots,$$

$$F_2 = \alpha^2 F_{20} + \alpha^3 F_{21} + \cdots,$$

$$m_2 = \alpha^2 m_{20} + \alpha^3 m_{21} + \ldots, \text{etc.}$$

Substituting these expansions in eqs. (15)–(18) and equating the coefficients of the various powers of α to zero we then obtain the following system of equations: (first set)

$$[xF_{00}''' + (1 + F_{00}) F_{00}'' - F_{00}'^2]' = 0, \tag{20a}$$

$$[xF_{10}''' + (1 + F_{00}) F_{10}'' - 4F_{00}'F_{10}' + 3F_{00}''F_{10}]' = 0, \tag{20b}$$

$$xm_{00}'' + F_{00}m_{00}' = 0, \tag{20c}$$

$$xm_{10}'' + F_{00}m_{10}' - 2F_{00}'m_{10} = -3F_{10}m_{00}' \tag{20d}$$

(second set)

$$[xF_{01}''' + (1 + F_{00})F_{01}'' - 2F_{00}'F_{01}' + F_{00}''F_{01}]'$$
$$= \frac{1}{2x^2}[m_{00}m_{10}] - 6F_{00}^2\left(\frac{x^{-1}F_{10}}{F_{00}}\right)' - 12F_{10}'', \tag{21a}$$

$$[xF_{11}''' + (1 + F_{00}) F_{11}'' - 4F_{00}'F_{11}' + 3F_{00}''F_{11}]' =$$
$$- (F_{01}F_{10}'' - 4F_{01}'F_{10}' + 3F_{01}''F_{10})' + \frac{1}{2x^2}(m_{10}^2$$
$$+ 2m_{00}m_{20}) - 6x^2\left(\frac{F_{10}^2}{x^3}\right)' - 20F_{00}\left(\frac{F_{20}}{x}\right)'$$
$$+ 60\frac{F_{00}'F_{20}}{x} - 40F_{20}', \tag{21b}$$

$$xm_{01}'' + F_{00}m_{01}' = -F_{01}m_{00}' - 2m_{10}, \tag{21c}$$

$$xm_{11}'' + F_{00}m_{11}' - 2F_{00}'m_{11} = -F_{01}m_{10}' + 2F_{01}'m_{10}$$
$$- 3(F_{10}m_{01}' + F_{11}m_{00}') - 12m_{20}, \tag{21d}$$

(Set 3, limited to F_{02} and m_{02} for brevity)

$$[xF_{02}''' + (1 + F_{00}) F_{02}'' - 2F_{00}'F_{02}' + F_{00}''F_{02}]'$$
$$= \frac{1}{2x^2}(m_{00}m_{11} + m_{01}m_{10}) + [-F_{01}F_{01}'' + F_{01}'^2]'$$
$$- 6F_{00}^2\left(\frac{F_{11}}{xF_{00}}\right)' - 6F_{01}^2\left(\frac{F_{10}}{xF_{01}}\right)' - 120\frac{F_{20}}{x}, \tag{22a}$$

$$xm_{02}'' + F_{00}m_{02}' = -2m_{11} - F_{01}m_{01}' - F_{02}m_{00}'. \tag{22b}$$

Eqs. (20a) and (20c) are found in Kuo (1969) while the latter equation also appears in Kuo (1966, 1967). Observe that eq. (20a) is nonlinear but contains F_{00} alone; hence it can be solved together with the boundary conditions to yield F_{00}, while all the other equations are linear and contain lower order functions as coefficients and non-homogeneous terms. Notice also that the inclusion of the F_1 term in (11) makes the tangential and the radial velocities coupled through eqs. (20d) to (22b).

3.3. *The boundary conditions*

At the axis we require that each of the variables be zero for the axisymmetric flow, i.e., at $x = 0$

$$m_{0i} = F_{0i} = 0, \qquad i = 0, 1, \cdots \tag{23}$$

$$m_{1i} = F_{1i} = 0, \qquad i = 0, 1, \cdots$$

At the rim, $x = x_s$, we assume the vertical velocity is zero, that the radial inflow will vary slightly with height while the rotation rate does not vary in the vertical. Also, we shall take all the radial inflow and rotation in the first term in the α expansion, and none in the higher perturbations. Therefore at x_s the solutions satisfy

$$F_{0i}' = 0, \qquad i = 0, 1, \cdots, \tag{24}$$

$$F_{0i} = 0, \qquad i = 1, 2, \cdots,$$

$$F_{0i}''' = 0, \qquad i = 0, 1, \cdots,$$

$$m_{0i} = 0, \qquad i = 1, 2, \cdots,$$

$$F_{1i}' = 0, \qquad i = 0, 1, \cdots,$$

$$F_{1i} = 0, \qquad i = 1, 2, \cdots,$$

$$F_{1i}''' = 0, \qquad i = 0, 1, \cdots,$$

$$m_{1i} = 0, \qquad i = 0, 1, \cdots,$$

while F_{00}, F_{10} and m_{00} are assigned non-zero values. The condition on the third derivative is needed to complete the requirement of four boundary conditions for the fourth order equations. Integrating (20a) from 0 to x_s, applying the boundary conditions given above and solving for $F''_{00}(x_s)$ yields

$$F''_{00}(x_s) = \frac{F''_{00}(0) - F'^2_{00}(0)}{(1 + F_{00}(x_s))}. \tag{25}$$

This relation shows that $F''_{00}(x_s)$ is non-zero if $F''_{00}(0) \neq F'^2_{00}(0)$. A similar procedure applied to eq. (20b) reveals that

$$F''_{10}(x_s) = \frac{F''_{10}(0) - 4F'_{00}(0)\,F'_{10}(0) - 3F''_{00}(x_s)\,F_{10}(x_s)}{(1 + F_{00}(x_s))}, \tag{26}$$

which is also non-zero if the numerator is non-zero.

At the rim the swirl angle θ can be written in terms of m_0 and F_0 since eqs. (12), (14) and the boundary conditions (24) give at the $z^* = 0$ level

$$\theta = -\tan^{-1}(v/u) = \tan^{-1}(m_0/2F_0).$$

Note also at the rim we have $m_0(x_s) = m_{00}(x_s)$ and $F_0(x_s) = F_{00}(x_s)$.

3.4. *Details of the numerical procedure*

The non-linear ordinary differential equations described by eqs. (20), (21) and (22) with their corresponding boundary conditions (23) and (24) are solved numerically, in the order listed above, using a shooting technique (Conte and de Boor, 1972). Each equation is rewritten as a system of first order equations and then discretized using the midpoint rule (Kreiss and Oliger, 1973). Thus, e.g., each fourth order equation is reduced to a system of four first order equations that must be solved iteratively. A fine grid is employed near the axis, e.g., $\Delta x = 10^{-4}$, but this spacing is allowed gradually to expand to a much coarser net near the rim, say $\Delta x = 10^{-1}$. As an example, a total of 575 grid points are used on the interval $x = 0$ to 20. Tests using nearly double this number of grid points yield no significant differences.

Utilizing a shooting technique to solve the fourth order differential equations for the various F's requires that initially a guess be made for the first and second derivatives at $x = 0$. Using these guesses the third derivative at $x = 0$ is then computed directly from the equation. The system of four first order equations are solved for all x using standard procedures and then the values for $F_{i,j}$ and its first derivative at $x = x_s$ are compared with the desired boundary conditions. If the differences exceed a specified small value, say 10^{-5}, the process is again repeated using new estimates to replace the values of the first and second derivatives at $x = 0$. These new values are obtained using Muller's method (Conte and de Boor, 1972).

We have only two degrees of freedom so the condition on the third derivative at the rim can not be strictly enforced but we accept only those solutions for which the required condition is naturally approximately satisfied, i.e., $F'''_{i,j} \simeq 0$, $i = 0, 1, \cdots, j = 0, 1, \cdots$ The error introduced by this procedure is quite small since, e.g., the calculated value of $F''_{00}(x_s)$ varies from that predicted by eq. (25) typically only in the fourth significant decimal place.

Our equations actually possess multiple solutions that satisfy all the above stated boundary conditions, e.g., two separate solutions for F_{00}, eq. (20a), are known to exist and more may be possible. Using initial guesses with $F'_{00}(0) > 0$ and $F''_{00}(0) < 0$ we obtain a solution which contains all positive values of F'_{00} (one cell vortex) while the second solution, obtained using initial guesses $F'_{00}(0) < 0$ and $F''_{00}(0) > 0$, contains negative values of F'_{00} near the axis and positive values further away (two cell vortices). Kuo (1967), examining a vortex in an unstably stratified atmosphere, shows similar two cell solutions for the special case when all the derivatives are zero at the rim. Our two cell solutions remain essentially unchanged near the axis as the rim is moved further and further away. This behavior is not observed in the laboratory vortex (Ward, 1972; Church *et al.*, 1979), so in this study we disregard this solution and utilize only initial guesses that satisfy $F'_{00}(0) > 0$ and $F''_{00}(0) < 0$. The exact magnitude for these choices depends on the strength of the inflow at the rim.

The solution of the m equation is straight forward and does not change significantly with the change of the vertical velocity at the axis and therefore it will not be presented here.

4. Discussion of results

In this study a similarity approach is utilized to obtain the solution of the two-dimensional nonlinear vortex equations for comparison with the results obtained from laboratory vortex simulators, so that the vertical and radial variations are uncoupled. For simplicity, the geometry of the vortex simulator is ignored and only the nature of the flow within the convergence or inflow region is investigated for a range of swirl angles. Care must be exercised in interpreting our results however since the similarity transform ignores the geometry and by limiting this study to within the convergence region we also ignore the source of the convergence, i.e., the exhaust fan, and thus there is no guarantee that different rim rotation rates, with the same specified radial inflow, will experience the same volume flow rate. Fortunately Davies-Jones (1973) has shown that within the experimental ranges for the three nondimensional quantities, namely, the radial Reynolds number, the aspect ratio and the swirl ratio, it is the swirl ratio that most strongly controls the laboratory vortex flow configuration. In our calculations, some small variations of the aspect ratio and radial Reynolds number are inherent because of the nature of the similarity approach, but these changes are thought to be minimal and should not distort the general conclusions. Also our model includes the viscous or diffusion terms but does not include the boundary layer explicitly since the motion predicted at $z^* = 0$ is non-zero and not the no-slip flow required in boundary layer theory. The zero value for z^* should be interpreted as occurring near the top of the surface boundary layer.

We will vary the boundary conditions at the rim ($x = x_s$) representing changes in the strength of the radial velocity or inflow ($F_{00}(x_s)$), the vertical variation of the radial velocity component ($F_{10}(x_s)$, $F_{20}(x_s)$, ...) and the strength of the rotation or tangential velocity ($m_{00}(x_s)$), and observe the predicted flow pattern. Note that the height dependency is determined by the first and higher order terms in eq. (11) and is established by the choice of boundary conditions at the rim. Results will be presented normally for two boundary parameters fixed while the third is varied over some range. The resulting flows may not always be observed since in the laboratory vortex there may be some natural compensation at the rim in the vertical variation, for example, as changes occur there in either the strength of the radial inflow or rotation rate. Nevertheless we can clearly show the trends produced by individual changes in these boundary parameters.

Our results illustrated in Figs. 1 through 11 are displayed in terms of the dimensional radial variable $r = r^*$ or in $(r^*)^{1/2}$ scale to better visualize the predicted flow pattern near the axis. The first 10 figures are for an intense vortex similar to those produced in modern laboratory vortex simulators. The outer rim is located at $r^*(x_s) = 1.932$ m while the last figure shows a weaker configuration with maximum radius of 0.642 m. Because the intensity of the inflow and rotation at the outer rim greatly affects the location of the maximum tangential velocity in the x coordinate an appropriate choice for r_0 must be established for each of the two cases to convert our calculations in x back into the $r = r^*$ scale. The scaling factor r_0 is calculated once for each case via the formula $x_{\mathrm{vmax}} = r^2_{\mathrm{vmax}} \cdot (2r_0)^{-2}$ by selecting 0.15 m as the appropriate radius for the maximum tangential velocity, in approximate agreement with laboratory simulations (Church *et al.*, 1979). Both radii given above correspond to a maximum value for x of 20. This value is selected as typical from a large number of tests. Using numerical results representative of each case the scaling factor for the more intense flow is determined as $r_0 = 0.215$ m while the weaker case uses $r_0 = 0.0728$ m. The equations for F_0, m_0, ..., themselves are independent of r_0, δ and ν but to convert back to the dimensional variables requires some appropriate choices. The radial distance is labeled r^* in the figures indicating that our choice of r_0 has been used to convert from the x coordinate back into the dimensional $r = r^*$ coordinate.

Radial profiles of F_0' and its components are shown in Fig. 1. These are computed using $F_{00}(x_s) = 250$, $F_{10}(x_s) = -0.8$ and $m_{00}(x_s) = 194$ and are presented in a uniform $(r^*)^{1/2}$ scale. F_0' and its components should be interpreted as a measure of the vertical velocity (eq. 13). The solid curve labeled F_{00}', obtained from (20a) has its maximum value at the axis, i.e. $r^* = 0$, and by itself is typical of the profile found in a one-cell vortex (Kuo, 1966). When higher order expansion terms, obtained from eqs. (21a) and (22a) are included in $F_0' = F_{00}' + \alpha F_{01}' = \alpha^2 F_{02}'$ with α taken as one, the profile is radically different since $F_0' \simeq 0$ at $r^* = 0$ and thus represents the initial stage of a two cell vortex. The latter is generally characterized by negative vertical velocities at and near the axis with non-negative values further away. For our purposes three terms will be sufficient to approximate

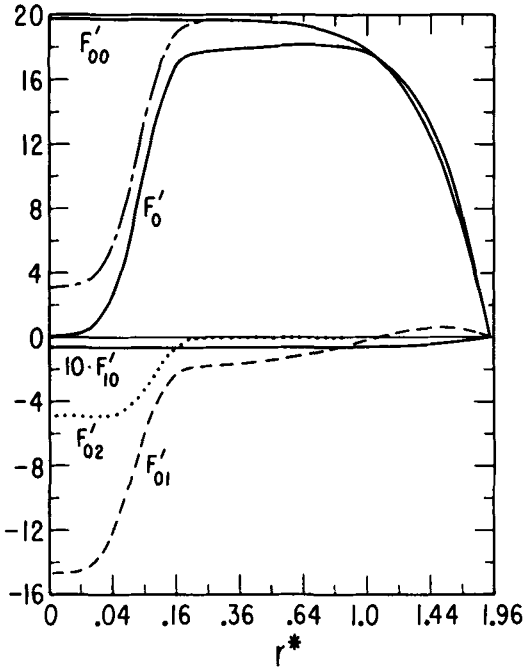

Fig. 1. Radial profiles of F'_0 which is proportional to the vertical velocity, and its components are given. F_{10} is also displayed. First subscript denotes the δz^2 expression while the second indicates location in α expansion. Boundary values: $F_{00} = 250$, $m_{00} = 194$ and $F_{10} = -0.8$. Dashed-dot curve is F'_0 when vertical diffusion is ignored.

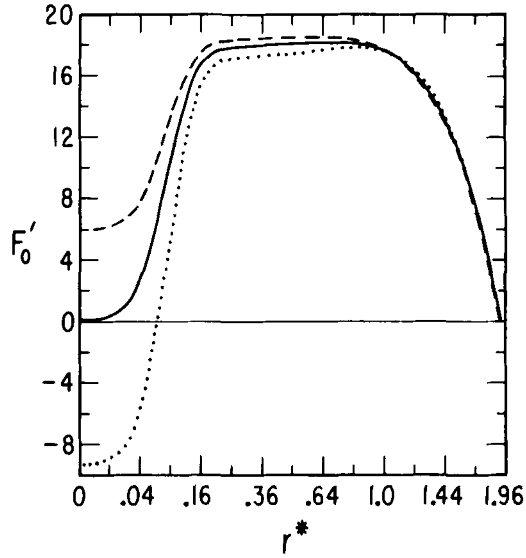

Fig. 2. Radial profiles of F'_0 computed using three different boundary values for F_{10}, i.e. (solid) $F_{10} = -0.8$, (dotted) $F_{10} = -1.1$ and (dashed) $F_{10} = -0.6$. Other boundary values same as in Fig. 1.

F_0 or F'_0, since e.g., the dotted curve representing F'_{02} is significantly smaller in magnitude than either F'_{00} or F'_{01} indicating the decreasing importance of higher order terms in the α expansion. Higher order terms in the (δz^{*2}) power series expansion, eqs. (10) and (11) like F_1, where $F_1 = \alpha F_{10} + \alpha^2 F_{11}$, are similarly much smaller than the zeroth-order terms. Note that $10 \cdot F'_{10}$ as plotted in Fig. 1 is still small in magnitude. The second term in F_1, i.e. F_{11}, is even smaller. We will neglect the very small contributions of F_2 and other higher order terms.

Included in Fig. 1 is the dashed-dot curve showing the radial profile of F'_0 when terms generated by vertical diffusion are removed from the calculations. The resulting differences in F'_0 are clearly small as seen by comparing the dashed-dot and solid curves and do not change the two cell nature of the vortex which results when radial and tangential motions are coupled. Our calculations show that as the vortex becomes more intense this small contribution is reduced even further (not displayed) while in the convergence region of a weak vortex vertical variations are more pronounced so that vertical diffusion becomes more important, as shown in Fig. 11. In this weaker vortex configuration, Fig. 11, the ratio of F_{10}/F_{00} at x_s is an order of magnitude larger than that used to compute the more intense vortex described in Figs. 1 through 10.

According to Hall (1972) the vortex core is characterized, above the boundary layer, by a slight spreading out of the core with height; hence a small decrease in radial and tengential velocities with height and the development of an adverse pressure gradient. We tune our model to produce similar behaviour by choosing F_1 as minutely negative at the rim, and hence negative over the entire radius, giving an increasingly negative contribution with increasing height to the radial velocity component and consequently to the tangential velocity. Fig. 2 shows that the value of F'_0 is sensitive to changes in F_1 since non-zero F_1 values allow the tangential velocity and radial motions to be coupled. If F_1 is identically zero everywhere, then F_0 will be identically F_{00}, i.e., the radial motion becomes independent of the rotation rate. The magnitude of F_1 is chosen so that the coupling

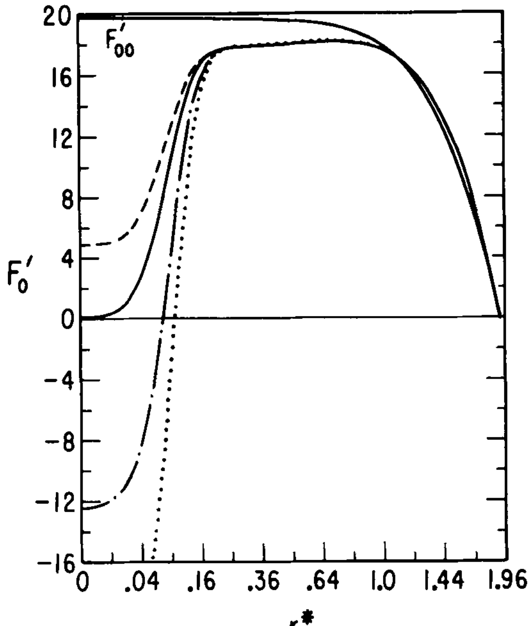

Fig. 3. Radial profiles of F_0' computed for four different swirl angles obtained by varying the tangential velocity. Boundary values used are (solid) $m_{00} = 194$, (dashed) $m_{00} = 170$, (dashed-dot) $m_{00} = 240$ and (dotted) $m_{00} = 280$. Other boundary values same as in Fig. 1.

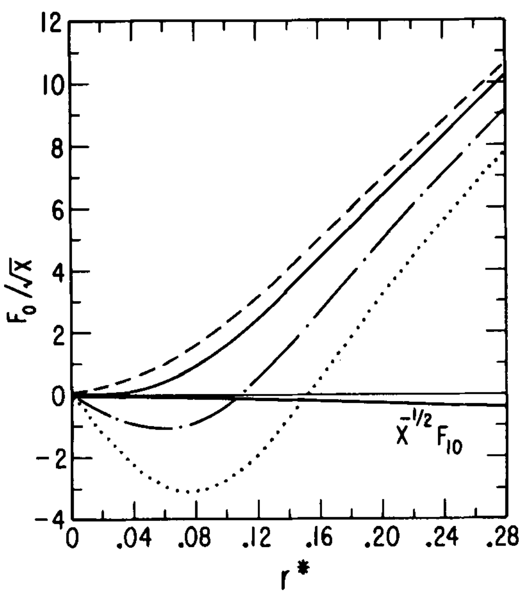

Fig. 4. Same as Fig. 3 except showing $x^{-1/2}F_0$, which is proportional to the radial velocity, on a linear scale near the axis.

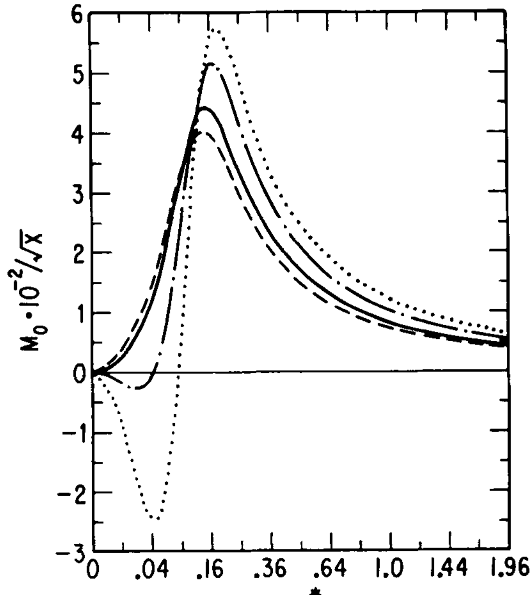

Fig. 5. Same as Fig. 3 except showing $x^{-1/2}m_0$ which is proportional to the tangential velocity.

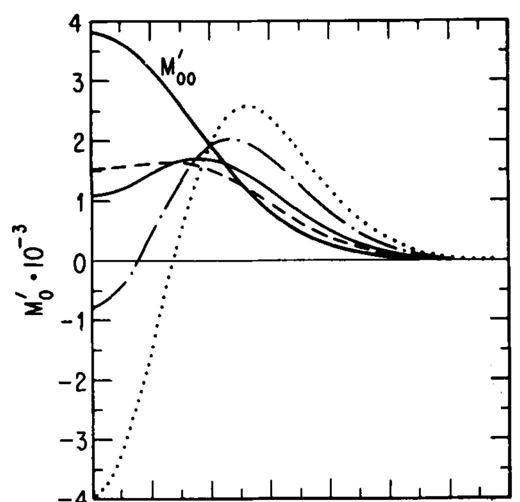

Fig. 6. Same as Fig. 3 except showing m_0' which is proportional to the vertical vorticity.

effects of F_1 and m_1 produce nearly zero values at the axis for F_0', solid line, when the swirl angle, $\theta = \tan^{-1} m_o/2F_0$, is in the neighbourhood of twenty degrees in approximate agreement with results found in laboratory simulations (Church *et al.*, 1979; Church and Snow, 1979).

In Fig. 3, radial profiles of F_0' are presented for four different rotation rates at the rim, i.e., with $m_{00}(x_s) = 170$, 194, 240 and 280 while $F_{00}(x_s) = 250$ and $F_{10}(x_s) = -0.8$ are each held fixed. This is equivalent to varying the swirl angle at the rim from 18.78° to 29.25° ($z^* = 0$) by adjusting the tangential velocity. It should be noted that laboratory simulations measure their swirl angle somewhere between the rotating screen and the updraft core and not at the rim exactly. For the smaller value of $m_{00}(x_s)$ of 170 the F_0' profile, given by the dashed curve, is positive throughout the entire radius but already significantly reduced near the axis as seen when compared with the solid curve labelled F_{00}' which does not include the coupling effect of the tangential flow. As the rotation rate is increased F_0' becomes increasingly smaller at the axis and is nearly zero when $m_{00}(x_s) = 194$ (solid line). Further increases in the rotation rate produce negative F_0' values at the axis typical of the two celled vortex. Note that the profile away from the axis, say $r^* > 0.25$ m, remains almost unaffected by variations in the swirl angle. In the laboratory simulator where the volume flow rate is unchanged in the experiment there would be somewhat more of an increase in this outer region, of the order of 10%, to compensate for the downward motion at the axis. Thus our results for increasing values of m_0 at the boundary have a small decreasing volume flow rate for the same radial inflow rate. This may be interpreted as having a slightly decreasing aspect ratio and radial Reynolds number. Consequently the swirl ratio S will increase more than that predicted due to changes in the swirl angle alone since S is inversely proportional to the aspect ratio.

In Fig. 4 values of $x^{-1/2}F_0$, which is proportional to the radial velocity, are given up to a radius of 0.28 m. The two cell flow is very evident in the dashed-dot ($m_{00} = 240$) and dotted curves ($m_{00} = 280$) since both have negative values next to the axis. The solid curve labeled $x^{-1/2}F_{10}$ shows the smallness of the negative first order term when compared with zero order terms.

The development of the downward vertical motion at the axis is clearly seen to descend from high levels of z, in agreement with laboratory findings (Church *et al.*, 1979), since negative vertical motion is possible when small positive zeroth-order and negative first-order terms are combined provided at some $z^* > 0$ the expression $|\delta z^* F_1'| > F_0'$ in eq. (13) is first satisfied. This occurs when F_0' is much subdued but still positive at the axis, e.g., as does occur as shown in Fig. 3. The combination of zeroth and first order terms would then lead to a reduction with height in the vertical velocity, a stagnation or zero point and finally negative vertical motion above that level. This type of motion is clearly seen in the laboratory simulations of the vortex (Church *et al.*, 1979; Ward, 1972).

Profiles of the tangential velocities are shown in Fig. 5 for the same cases discussed in Figs. 3 and 4. As the swirl angle at $z^* = 0$ is increased in value for four cases between 18.78 to 29.25°, corresponding to the dashed through dotted curves respectively, the tangential velocity maximum moves further from the axis, a feature commonly observed in laboratory simulations (Church *et al.*, 1979). Outside the radius of maximum tangential flow the shapes of the profiles are very similar. This follows since the value of the zeroth order angular momentum, $m_0 = v_0 r$, remains nearly constant. For example with a value of 194 at the rim, the value of m_0 is 192.8 at $r^* = 0.2422$ m which is very close to the radius of maximum velocity at 0.15 m. This means that the vertical vorticity is confined within a region certainly less than twice the radius of the maximum tangential velocity. The flow behaviour very near the axis is in a state of near solid rotation; thus F_0, m_0, ... each are nearly proportional to x as shown in Table 1 for the case $m_{00}(x_s) = 194$. Obviously the slope there will vary as the swirl angle is changed. Note that as $m_o(x_s)$ is increased from 170 to 194, dashed and solid line respectively

Table 1. *Values at two locations near the axis for various components of F_0 and F_1, along with m_0 and m_1 showing the linear relationship with respect to x*

x	r^*	F_{00}	F_{01}	F_{02}	F_{10}	F_0	F_1	m_0	m_1
0.0001	0.0043	0.00196	−0.00146	−0.00049	−0.000006	0.000011	−0.000009	0.10736	−0.00165
0.001	0.01359	0.01967	−0.01453	−0.00499	−0.000064	0.00015	−0.000086	1.09742	−0.01626

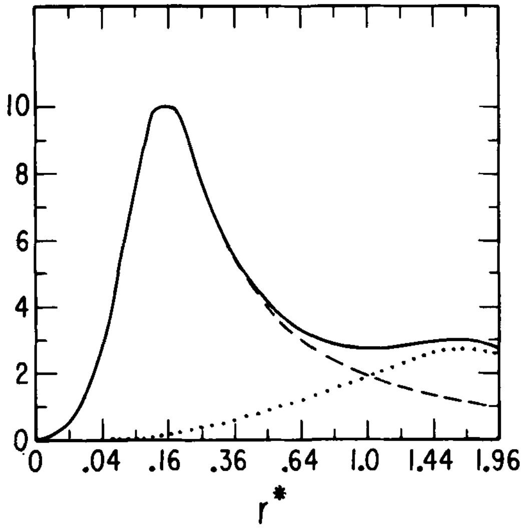

Fig. 7. Radial profiles (time 10^{-2}) of $(u^2 + v^2)^{1/2}\nu^{-1}$ (solid), $v\nu^{-1}$ (dashed) and $u\nu^{-1}$ (dotted). Boundary values same as used in Fig. 1.

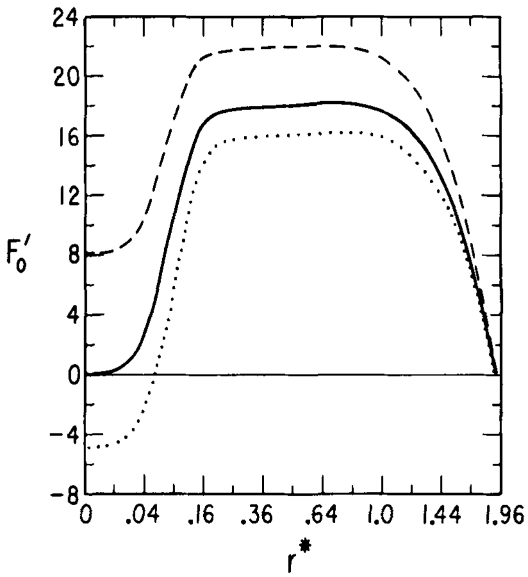

Fig. 8. Radial profiles of F_0' for three swirl angles obtained by varying the radial velocity component. Boundary values: (solid) $F_{00} = 250$, (dashed) $F_{00} = 300$ and (dotted) $F_{00} = 225$. Other boundary values same as Fig. 1.

in Fig. 5, the slope of the tangential velocity is slightly reduced near the axis but enhanced as it approaches its maximum value. Further increases in the swirl angle continue to steepen the slope just inside the radius of maximum velocity.

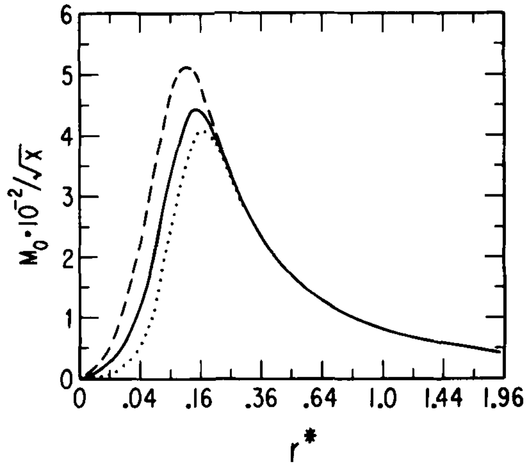

Fig. 9. Same as Fig. 8 except showing $x^{-1/2}m_0$.

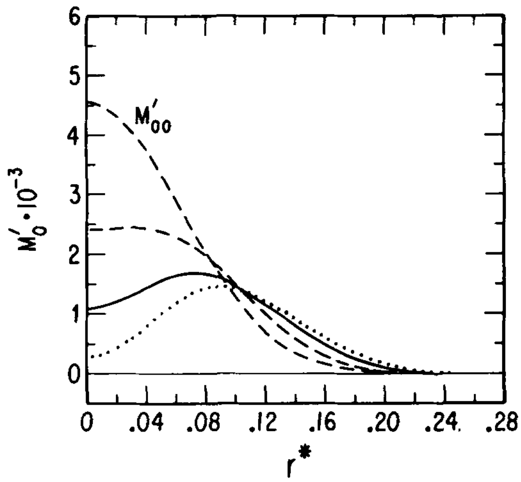

Fig. 10. Same as Fig. 8 except showing m_0'.

The tangential velocity is observed to become negative in the region of the core where the two cell vortex contains negative vertical velocity and outward radial velocity and hence gives rise to an advective loss of angular momentum in the core. In the laboratory simulator the downward motion at the axis in the two cell vortex appears to descend downward through the baffling near the top of the vortex generator down to the lower surface. Obviously our model which is restricted to the convergence region of the vortex cannot duplicate this behaviour. The configuration given by the dashed-dot and dotted curves in Fig. 5, representing predicted rotational flow for a two celled vortex, will give rise to inertial instability since the gradient of the circulation changes signs (Rayleigh, 1916; Synge, 1938).

Another type of instability is revealed in Fig. 6 by the radial profiles of m_0'; here m_0' is proportional to the vertical vorticity and the prime denotes a derivative with respect to x. Even for the smaller boundary value of $m_{00}(x_s) = 170$ (dashed curve) the gradient of m_0' changes sign revealing that the flow configuration is barotropically unstable. The slope of the uncoupled or zeroth order term m_{00}' is of the same sign; thus the instability portrayed in other curves arises because of the coupling effect of the radial and vertical flows back on the tangential motion. Note that the maximum value for m_{00}' occurs at the axis while in the other curves, representing m_0' for increasing swirl angles, the maxima are achieved progressively further away from the axis and closer to the tangential velocity maxima. In fact these maxima occur where the gradient of the tangential velocity is very large as seen when comparing Figs. 5 and 6. These results indicate that azimuthally varying three-dimensional disturbances precluded from the present axisymmetric model will be created under these unstable conditions, which will even out the negative vorticity and negative rotation in the core to make them not observable in laboratory simulation. The possibility that barotropic instability of the tangential flow profile may lead to generation of suction vortex type disturbance in tornadoes as suggested by Fujita (1972) has been investigated by Staley and Gall (1979). Snow (1978) has postulated the other alternative, i.e., an inertial instability.

The radial profile of the scaled velocity magnitude $(|V|\nu^{-1}\cdot 10^{-2})$ at level $z = 0$ and its tangential and radial component are represented by the continuous, the dashed and the dotted curves in Fig. 7 respectively. This form of presentation is taken since a conversion to actual velocity would require knowledge of the viscosity coefficient ν. Our model predicts less than a four-fold increase in the velocity magnitude from the rim to its maximum value. This appears to agree very well with laboratory simulations (Church *et al.*, 1979). Also note that the radial component's contribution to the velocity magnitude is very small inside the radius of maximum tengential velocity but dominates near the rim.

For very small swirl angles (not shown), our model, in agreement with laboratory findings (Snow *et al.*, 1980) gives weakly swirling flows without a central core. In this case the tangential component increases with radius right up to the rim.

Radial profiles proportional to the vertical velocity, the tangential velocity and the vertical vorticity are shown in Figs. 8 through 10, respectively. Three different values of the swirl angle ranging from 17.92 to 23.32° ($z^* = 0$) are used by varying the radial inflow component while keeping the rotation rate at the rim constant. As the boundary value of F_{00} is decreased from 300 (dashed curve) to 225 (dotted curve) while $m_{00}(x_s) = 194$ and $F_{10}(x_s) = -0.8$ are each held constant, the vertical flow is found to change from all positive values to the two cell configuration, in agreement with what happens as the swirl angle is increased. Correspondingly, the tangential velocity (Fig. 9) shows a decrease in magnitude with an outward expansion of the radius of the maximum value in accordance with the law of conservation of angular momentum. The curves in Fig. 10 show a similar pattern to those discussed earlier for the vertical vorticity.

Our equations are non-linear so the nature of their solutions might vary somewhat as the magnitudes of the boundary values are varied but we find that for a large range of boundary conditions they still behave similarly. A weaker flow configuration using $F_{00}(x_s) = 25$ is shown in Fig. 11, but even in this case it still is possible to have the

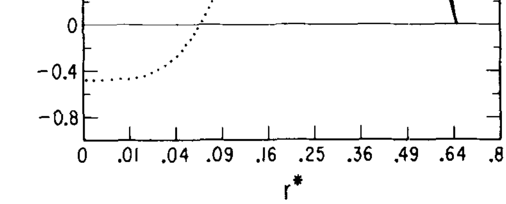

Fig. 11. Radial profiles of F_0' for three swirl angles. Computed using boundary values (solid) $m_{00} = 20$, (dashed) $m_{00} = 10$ and (dotted) $m_{00} = 30$. Otherwise $F_{00}(x_s) = 25$ and $F_{10}(x_s) = -0.3$. The dashed-dot curve is F_0' when vertical diffusion is ignored.

vertical velocity change from all positive (dashed line, $m_{00}(x_s) = 10$) to that found in a two-celled vortex (dotted line, $m_{00}(x_s) = 30$) by changing the tangential velocity at the rim. No negative tangential velocities are generated for this case where the swirl angle is varied from 11.31 to 30.96°. Tests using $F_{00}(x_s) = 500$ also generate the two-celled vortex with the appropriate choices of $m_{00}(x_s)$. Note that when our results are converted into actual velocities, the choice for the value of viscosity, used in scaling the equation, does not determine the nature of the flow since the same flow characteristics are found over a broad range of boundary values.

5. Conclusion

In this study, a model of the convergence region of a laboratory vortex is investigated via a similarity approach. The predicted flow is shown to vary significantly only near the axis as the swirl angle at the outer rim is changed. This type of response appears to be exactly similar to that observed in the laboratory. Of course, not all the details of the flow found in the laboratory vortex generator can be reproduced here, but the nature or trend of changes predicted in this study appears to be generally valid.

6. Acknowledgement

This research is supported by Air Force Geophysics Laboratory through Contract No. F19628-80-C-0012.

REFERENCES

Agee, E. M., Church, C. R., Morris, C. and Snow, J. T. 1975. Some synoptic aspects and dynamic features of vortices associated with the tornado outbreak of 3 April 1974. *Mon. Wea. Rev. 103*, 318–333.

Church, C. R., Snow, J. T. and Agee, E. M. 1977. Tornado vortex simulation at Purdue University. *Bull. Amer. Meteorol. Soc. 58*, 900–908.

Church, C. R. and Snow, J. T. 1979. The dynamics of natural tornadoes as inferred from laboratory simulations. *J. Rech. Atmos. 13*, 111–133.

Church, C. R., Snow, J. T., Baker, G. L. and Agee E. M. 1979. Characteristics of tornado-like vortices as a function of swirl ratio: a laboratory investigation. *J. Atmos. Sci. 36*, 1755–1776.

Conte, S. D. and deBoor, C. 1972. *Elementary numerical analysis: an algorithmic approach.* New York: McGraw-Hill, 396 pp.

Davies-Jones, R. P. 1973. The dependence of core radius on swirl ratio in a tornado simulator. *J. Atmos. Sci. 30*, 1427–1430.

Davies-Jones, R. P. and Kessler, E. 1974. *Tornadoes, weather and climate modification* (ed. W. N. Hess). Wiley, 842 pp. (See chap. 16.)

Forbes, G. S. 1978. Three scales of motion associated with tornadoes. Ph.D. Thesis, Univ. of Chicago, Chicago, Illinois. 359 pp. [Available from National Technical Information Service, Springfield, Virginia 22161.]

Fujita, T. T. 1971. Proposed mechanism of suction spots accompanied by tornadoes. *Preprint, Seventh Conf. Severe Local Storms*, Boston: Amer. Meteorol. Soc. pp. 208–213.

Fujita, T. T. 1972. Proposed mechanism of suction spots accompanied by tornadoes. SMRP Research Paper No. 102, The University of Chicago, 14 pp.

Hall, M. G. 1972. Vortex breakdown. *Ann. Rev. Fluid Mech. 4*, 195–213.

Harlow, F. H. and Stein, L. R. 1974. Structural analysis of tornado-like vortices. *J. Atmos. Sci. 31*, 2081–2098.

Jischke, M. C. and Parang, 1974. Properties of simulated tornado-like vortices. *J. Atmos. Sci. 31*, 506–512.

Kreiss, H. and Oliger, J. 1973. Methods for the approximate solution of time dependent problems. WMO 11 CSN Joint Organizing Committee, GARP Publication Series No. 10, 107 pp.

Kuo, H. L. 1966. On the dynamics of convective atmospheric vortices. *J. Atmos. Sci. 23*, 25–42.

Kuo, H. L. 1967. Note on the similarity solutions of the vortex equations in an unstably stratified atmosphere. *J. Atmos. Sci. 24*, 95–97.

Kuo, H. L. 1969. Axisymmetric flows in the boundary layer of a maintained vortex. University of Chicago, Planetary Circ. Proj., Rept. No. 15, 54 pp.

Leslie, F. W. 1977. Surface roughness effect on suction vortex formation: a laboratory simulation. *J. Atmos. Sci. 34*, 1022–1027.

Lewellen, W. S. 1962. A solution for three-dimensional vortex flows with strong circulation. *J. Fluid Mech. 14*, 420–432.

Rayleigh, Lord 1916: On the dynamics of revolving fluids. *Proc. Roy. Soc. London*, A93, 148–154.

Rotunno, R. 1977. Numerical simulation of a laboratory vortex. *J. Atmos. Sci. 34*, 1942–1956.

Rotunno, R. 1979. A study of tornado-like vortex dynamics. *J. Atmos. Sci. 36*. 140–155.

Snow, J. T. 1978. On inertial instability as related to the multiple-vortex phenomenon. *J. Atmos. Sci. 35*, 1660–1677.

Snow, J. T. Church, C. R. and Barnhart, B. J. 1980. An investigation of the surface pressure fields beneath simulated tornado cyclones. *J. Atmos. Sci. 37*, 1013–1026.

Staley, D. O. and Gall, R. L. 1979. Barotropic instability in a tornado vortex. *J. Atmos. Sci. 36*, 973–981.

Synge, J. L. 1938. On the stability of a viscous fluid between rotating coaxial cylinders, *Proc. Roy. Soc. London Ser. A, 167*, 250–256.

Turner, J. S. and Lilly, D. K. 1963. The carbonated water tornado vortex. *J. Atmos. Sci. 20*, 468–471.

Ying, S. J. and Chang, C. C. 1970. Exploratory model study of tornado-like vortex dynamics. *J. Atmos. Sci. 27*, 3–14.

Ward, N. B. 1970. The exploration of certain features of tornado dynamics using a laboratory model. NOAA Tech. Mem. ERLTM-NSSL 52, 22 pp.

Ward, N. B. 1972. The exploration of certain features of tornado dynamics using a laboratory model. *J. Atmos. Sci. 29*, 1194–1204.